Hot Extrusion of Zircaloy-4 tubes : Induced Crystallographic Textures and Influence of the Initial Microstructure

R.E. Logé, Y.B. Chastel, M.Y. Perrin
Ecole des Mines de Paris – CEMEF
BP207, 06904 Sophia Antipolis Cedex, France
loge@spinach.mae.cornell.edu

J.W. Signorelli, R.A. Lebensohn
Instituto de Fisica Rosario (IFIR – CONICET)
27 de Febrero 210 Bis, 2000 Rosario, Argentina

ABSTRACT

Hot extrusion of Zircaloy-4 tubes usually starts from beta-quenched microstructures and induces strong textures. Individual crystallographic orientations were investigated, using the EBSP technique as well as TEM Kikuchi patterns. Basal poles were found close to the tangential direction of the tubes in regions exhibiting Fine and Homogeneously Distributed Precipitates (FHDP). In contrast, regions with Large and Isolated Precipitates (LIP) had more variable orientations.

Laboratory plane strain compression tests were performed and the induced textures were compared to numerical simulations using a polycrystalline viscoplastic self-consistent model. The beta-quenched material was modeled as a mixture of LIP and FHDP regions, each having a different set of slip system hardnesses, with a volume fraction depending on the previous thermal history. The model was subsequently applied to the prediction of texture evolution during extrusion with metadynamic recrystallization taking place thereafter. The calculation suggests that recrystallization modifies the orientation of those grains where <c+a> crystallographic slip has been significantly activated during deformation.

I. INTRODUCTION

Zircaloy-2 and Zircaloy-4 products have found a large range of applications in the nuclear industry, due to their low probability of neutron capture and their resistance to high temperature corrosion. In the sequence of forming processes leading to planar or tubular products, particular attention is usually paid to the induced crystallographic textures, as they dictate the extent of mechanical anisotropy of the final product. Indeed, Zircaloys are made primarily of zirconium (see Table 1) whose hexagonal symmetry (hcp) lattice exhibits both elastic and plastic anisotropy (1,2).

	Sn	O	Fe	Cr	Ni
Zircaloy-4	1.5	0.11	0.21	0.12	< 0.005
Zircaloy-2	1.5	0.11	0.13	0.12	0.05

Table 1 : chemical compositions of Zircaloy-2 and Zircaloy-4 (wt %).
The balance zirconium content is about 98 wt %.

Intermediate stages of forming processes of Zircaloy products are usually carried out in the high α-region, i.e. close to the phase transition between the hcp α-phase and the body-centered cubic (bcc) β-phase, around 1083 K. Textures resulting from hot rolling (3-5) or extrusion (6-9) of zirconium-based alloys have been studied in detail. However, slight variations in the forming process conditions (temperature or friction) or in the initial microstructure sometimes induce substantial texture modifications (9,10). The role of temperature is particularly unclear since it influences both the relative slip system hardnesses (2,11,12] and the proportion of recovery and/or recrystallization (10,13).

Hot extrusion of Zircaloy tubes usually involves dynamic recovery, and *metadynamic* recrystallization[1] (7,10,13). The extent of these phenomena vary along the radial direction of the tubes, due to both the thermo-mechanical conditions of the process and the initial microstructure. For example, metadynamic recrystallization proceeds after extrusion, upon air cooling of the tube, as long as the temperature is in the good temperature range. The cooling rates are typically of a few degrees per second, but vary along the radial direction. On the other hand, the *initial* microstructural gradient (i.e. before extrusion) comes from the water-quenching, or "**β-quenching**", operation. This quenching operation is performed on cylinders being heat treated in the β-phase. Only after this operation is done, is the cylinder drilled into a tube, and ready for extrusion. The cooling rate from the β-phase varies along the radial direction and dictates the type of *Widmanstätten* microstructure thereby obtained (15,16).

---

[1] *Metadynamic* recrystallization designates here the particular mechanism by which the structure starts recrystallizing right after deformation (no incubation period), provided that the temperature remains high enough. This kind of recrystallization initiates, like static recrystallization, only after some amount of deformation. However, unlike pure static recrystallization, its extent is also strongly related to the deformation *rate* applied to the material (14). The deformation rate is assumed to influence the number of recrystallization nuclei formed during deformation.

In this paper we focus on the effect of the β-quenched microstructure on the hot extrusion textures of Zircaloy-4 (**Zy4**) tubes, in the 873-1023 K temperature range. The extrusion deformation path along the inner boundary of a tube is approximated by that of laboratory plane strain compression (**PSC**) tests. In these tests, two types of initial microstructure, typical of low and high cooling rates from the β-phase, are chosen to study the microstructure effects on texture evolution. Metadynamic recrystallization is avoided in most cases by using a constant, and low enough deformation rate. Parallel to the PSC tests, the microstructures of hot extruded samples are examined, and related to measurements of individual crystallographic orientations. A viscoplastic self-consistent polycrystalline model (17) is then extended to include the observed relevant microstructural features in texture calculations. The model is calibrated with respect to the PSC tests, and then used to predict extrusion textures. The complication arising from the recrystallization effects is finally discussed, as well as the physical interpretation of the selected set of slip system hardnesses.

II. EXPERIMENTAL WORK

This study used a set of Zy4 cylinders which had been heat treated in the β-phase at 1323 K and subsequently water quenched. The experimental work involved laboratory mechanical testing, i.e. PSC tests, as well as industrial hot extrusion tests. The PSC samples were cut from a single cylinder, either close to the external surface or far from it, giving two categories : the Rapidly Quenched (**RQ**) samples and the Slowly Quenched (**SQ**) samples, respectively. Hot extrusion tests were performed on tubes obtained by drilling along the center line of the β-quenched cylinders, as explained earlier.

II.1. Initial Microstructure and Texture.

The microstructure varies along the radial direction of the cylinder, as a function of the cooling rate from the β-phase. Two extreme cases are given by the SQ and RQ microstructures described above. They are illustrated in Figure 1, using both optical microscopy and TEM.

With an optical microscope, the dependence of the platelet thickness on the cooling rate is clear (15). As seen from TEM images, precipitates are formed during cooling from the β-phase because of the very low solubility of both Fe and Cr in the α phase. In the SQ microstructures most of the precipitate volume fraction is made of Large and Isolated Precipitates (**LIP**), because the slow cooling rate allowed for some coarsening of the precipitates. In contrast, the RQ microstructure displays high volume fractions of Fine and Homogeneously Distributed Precipitates (**FHDP**) inside the platelets, while coarser precipitates still appear at their boundaries. Some coarse precipitates also rarely appear inside the platelets, but they should not be confused with

the long hydrides which have grown perpendicular to the platelet boundaries. Those hydrides form at low temperature, and dissolve well before reaching the high α-region.

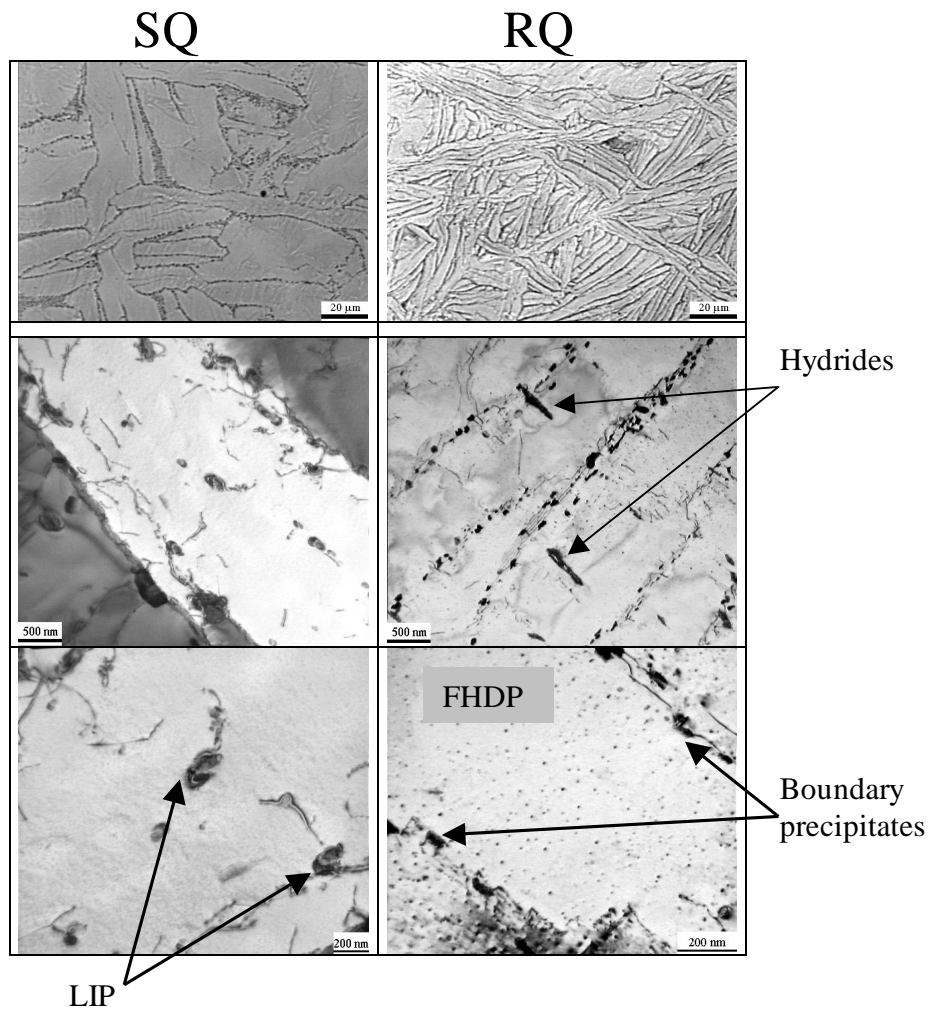

Figure 1 : Widmanstätten structures at different scales. RQ and SQ refer to Rapidly and Slowly Quenched from the β-phase, respectively.

Figure 2 shows how the initial texture varies along the thickness of the cylinder, which in turn gives the initial SQ and RQ textures, together with an intermediate one, at mid-thickness. The (0002) pole figures exhibit several peaks of high intensity, but distributed quite randomly. The peaks can be attributed to colonies of α platelets which grew, upon quenching, from large β grains, retaining close crystallographic orientations (18).
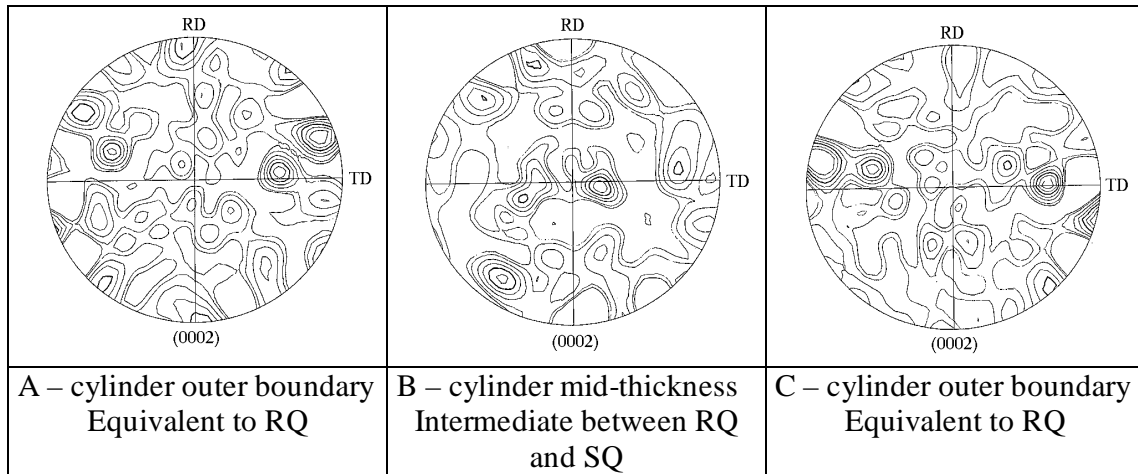
Mathematical Modeling in Metal Processing and Manufacturing (CD-ROM),
P. Martin and W.J. Liu, S. MacEwen, Y. Verreman and J. Goldak eds.
The Metallurgical Society of CIM, Canada, 2000.

A – cylinder outer boundary Equivalent to RQ	B – cylinder mid-thickness Intermediate between RQ and SQ	C – cylinder outer boundary Equivalent to RQ

Figure 2 : Three initial (0002) pole figures at 3 different thickness levels in a β-quenched cylinder.

II.2. Plane Strain Compression Tests (PSC Tests).

As stated earlier, PSC tests were used to study the effect of a "rolling" deformation mode on texture evolution, without the complication of recrystallization phenomena if the combination of strain rate and temperature is well chosen. The plane strain deformation mode is used as a representation of the deformation path along the inner surface of a tube being extruded.

II.2.1. Experimental Set-up

Figure 3 shows the experimental configuration with the dimensions of the tools and of the samples. These dimensions ensure a deformation mode close to ideal plane strain (19) in the deformed zone, all the way to the final thickness of 2.2 mm (62 % reduction).
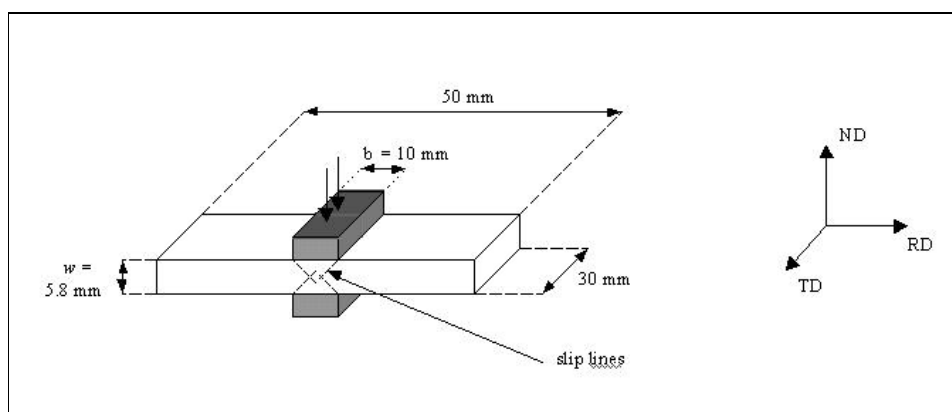

Figure 3 : PSC configuration.

Mathematical Modeling in Metal Processing and Manufacturing (CD-ROM),
P. Martin and W.J. Liu, S. MacEwen, Y. Verreman and J. Goldak eds.
The Metallurgical Society of CIM, Canada, 2000.

Tests were carried out at temperatures of 873, 923, 973 and 1023 K, and at strain rates of 0.1 s^{-1} and 1 s^{-1}, both for SQ and RQ samples. Reaching a homogeneous temperature took about 15 minutes so that samples were deformed only after some annealing. After deformation, the samples were air cooled and the crystallographic texture was systematically measured at mid-thickness of the specimens. Going from 0.1 s^{-1} to 1 s^{-1} did not significantly change the results in terms of texture evolution or microstructure evolution.

II.2.2. Final Textures

Figure 4 gives the three different types of (0002) pole figures obtained after PSC tests. The first type (A) is the most common one and refers to SQ samples. Most of the *c*-axes are close to the ND. The second and third types (B, C) refer to RQ samples. In these cases, a texture component appears with c-axes close to the TD (from now, we shall call this component a **"T"** texture component). At 923 K, other maxima appear close to the RD as well (B), but they disappear at 1023 K (C).

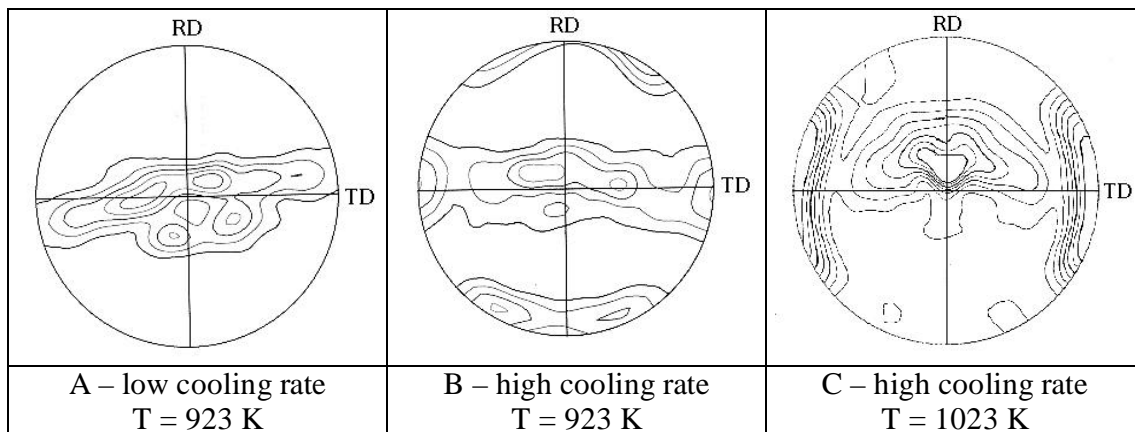| A – low cooling rate T = 923 K | B – high cooling rate T = 923 K | C – high cooling rate T = 1023 K |

Figure 4 : Typical (0002) pole figures obtained after PSC test. The samples were previously cooled from the β-phase at (A) low or (B)-(C) high rate (SQ and RQ microstructures, respectively), and deformed at various temperatures. The RD, TD and ND directions refer to those shown in Figure 3. Level lines are given in (A)-(B) multiples of random distribution (mrd), and (C) 0.5 mrd.

II.2.3. Recrystallization

Samples deformed in the 873-973 K interval retained the lamellar character of the initial Widmanstätten structure. This indicates that no recrystallization took place during or after deformation. Samples deformed at 1023 K, however, showed a non-negligible volume fraction of recrystallization. This means that, with strain rates of 0.1 s^{-1} and 1 s^{-1}, the effects of deformation and recrystallization could only be decoupled at temperatures less or equal to 973 K.

II.3. Analysis of Individual Crystallographic Orientations in Extruded Samples, as a Function of the Microstructure

The PSC tests led most of the time to non-recrystallized microstructures with high dislocation densities. TEM observations of such materials are therefore not easy, and crystallographic orientations are difficult to identify from TEM or EBSP Kikuchi patterns. On the contrary, extruded samples have a lower dislocation density because of metadynamic recrystallization and dynamic recovery. The thermally activated processes may of course influence grain crystallographic orientations. In what follows, both the thermally activated processes and the β-quenched microstructural features are investigated in their relationship with grain orientations.

II.3.1. Linking Crystallographic Orientations to Chemical Composition using EBSP/EDX Techniques

Eighty-three EBSP measurements were performed and are summarized in Figure 5. The global (0002) pole figure is split in two parts. The splitting procedure depends on the results of a chemical analysis obtained from the Electron Diffraction X-ray (EDX) technique, in the neighborhood of the area where the crystallographic orientation was measured. If a line-scan across the area showed smooth, non-negligible variations of Fe and/or Cr content, then the structure was assumed to exhibit, locally, variations of precipitates density. The corresponding area was labeled "FHDP-area", in reference to the initial microstructure (see section II.1.1). Figure 6 illustrates such a FHDP-area, with variations of Fe content. The measured spot for crystallographic orientation is indicated by a cross in the middle of the line-scan.

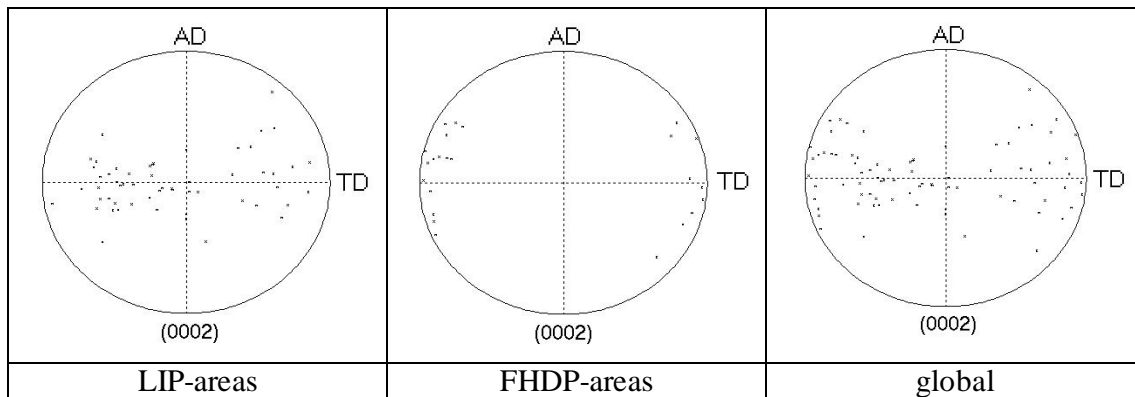| LIP-areas	FHDP-areas	global

Figure 5 : (0002) and $(10\bar{1}0)$ poles from EBSP measurements. Distinction is made between LIP-areas and FHDP-areas.

If, on the contrary, only random, discrete and strong peaks of Fe and/or Cr appeared, then the structure was assumed to contain only a few large and isolated precipitates, and the area was labeled "LIP-area" (see section II.1.1).

Mathematical Modeling in Metal Processing and Manufacturing (CD-ROM),
P. Martin and W.J. Liu, S. MacEwen, Y. Verreman and J. Goldak eds.
The Metallurgical Society of CIM, Canada, 2000.

Figure 5 shows that, with the distinction made from the EDX analyses, the "T" texture component clearly appears to be connected to FHDP-areas.
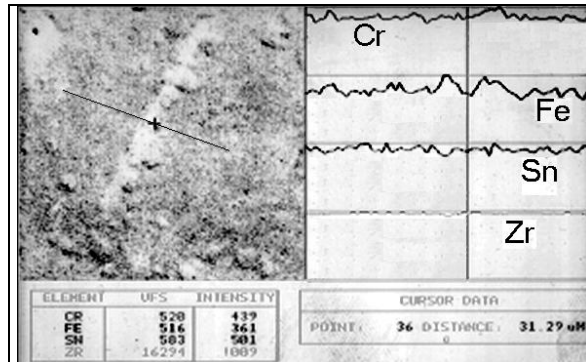

Figure 6 : Typical EDX line-scan showing variations of Sn-, Fe- and Cr-concentrations in an extruded sample, across a FHDP-area.

II.3.2. <u>Linking Individual Crystallographic Orientations to Dislocation Density and Precipitates Structure, using TEM Observations and Kikuchi Patterns</u>

Individual crystallographic orientations were determined from Kikuchi lines patterns, using the EDTEM code developed by S. Zaefferer (20). Several zones were analyzed, in order to identify possible rules linking the grain microstructural state to the "T" orientation, i.e. the FHDP-areas orientation in Figure 5.

Figure 7 gives the result of the analysis for ninety-four grains over an area of about 300 μm^2 corresponding to only a few platelets of the initial microstructure (see section II.1.1). It is shown here that these ninety-four grains reasonably account for the global (0002) pole figure, which indicates that a grain refinement has taken place and has led to very distinct orientations. Indeed the substructure formed within the former platelet structure is made of highly misoriented neighboring grains.

The observed grain structure refinement is the consequence of dislocation structure reorganizations taking place during and after deformation, which may influence the final texture. We therefore measured grain dislocation densities and tried to correlate them to crystallographic orientations. The result was negative. Instead of looking at the dislocation densities, we then examined the distribution of precipitates. FHDP and LIP grains were considered separately and, even if this distinction was not always easy to make, we found that most of the typical FHDP grains had a "T" orientation. We thus confirmed with this TEM study that the FHDP-areas previously measured on the SEM indeed correspond to regions exhibiting Fine and Homogeneously Distributed Precipitates.

Mathematical Modeling in Metal Processing and Manufacturing (CD-ROM),
P. Martin and W.J. Liu, S. MacEwen, Y. Verreman and J. Goldak eds.
The Metallurgical Society of CIM, Canada, 2000.

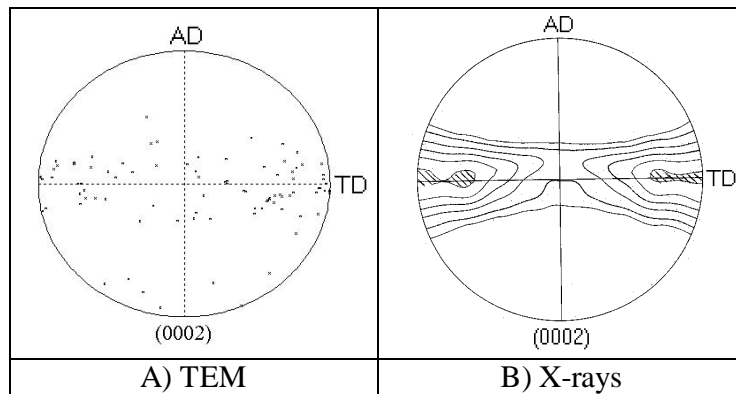| A) TEM	B) X-rays

Figure 7 : (0002) extrusion pole figures corresponding to : (A) measured individual grain orientations using TEM, and (B) a global X-ray measurement.

III. TEXTURE CALCULATION

III.1. The Polycrystalline Viscoplastic Self-consistent Model

The self-consistent model developed by (17) was used to calculate texture evolution. The initial texture was represented by a set of 1000 random orientations with equal weights, as it is usually observed that the β-quenching operation more or less randomizes the texture (see Figure 2).

As in (21) the assumed active deformation modes are $\{10\bar{1}0\}<1\bar{2}10>$ prismatic slip, $\{0001\}<1\bar{2}10>$ basal slip, $\{10\bar{1}1\}<1\bar{2}10>$ pyramidal slip in the <a> direction, and $\{10\bar{1}1\}<11\bar{2}3>$ pyramidal slip in the <c+a> direction. These deformation modes will be referred to as pr<a>, bas<a>, pyr<a> and pyr<c+a>, respectively.

III.2. Plane Strain Compression Test

In principle, the velocity gradient matrix describing the PSC test is complex, due to the friction effects. However, the simulation was used to reproduce the microstructure effects on texture evolution, reported on Figure 4. The influence of friction effects was therefore neglected for this purpose.

Simulations in (5) have already shown that it is possible to match the (0002) pole figure of Figure 4A, with a realistic set of CRSS. The other two pole figures in Figure 4B,C are not as easy to reproduce. An inverse method developed by (22) was applied to the latter experimental results to decide if any selection of CRSS may produce the required texture components, assuming the four active slip systems described previously, and a microscopic strain rate sensitivity of 0.14. The result of the calculation was

Mathematical Modeling in Metal Processing and Manufacturing (CD-ROM),
P. Martin and W.J. Liu, S. MacEwen, Y. Verreman and J. Goldak eds.
The Metallurgical Society of CIM, Canada, 2000.

negative, which might be attributed to some inadequacy of the self-consistent model. However, the microstructure examinations reported in section II have shown that it is meaningful to consider the β-quenched material as made of two different classes of grains, the LIP and FHDP grains. As the deformation proceeds, they systematically form distinct texture components, and must therefore have distinct properties. The β-quenched material is in that respect *heterogeneous*. Consequently, the *two-phase* version of the model was used, taking the CRSS reported in (5) for LIP regions and a new set of CRSS for FHDP regions. In the latter regions, the effect of iron was thought to favor pyramidal slip, as will be discussed later. Since prismatic slip is always the principal deformation mode in zirconium alloys, pr<a>, pyr<a> and pyr<c+a> slip systems were considered active in FHDP regions, but the basal slip systems were not. The best fit with experimental results was obtained with the CRSS values reported in Table 2.

	Pr<a>	Bas<a>	Pyr<a>	Pyr<c+a>
LIP regions	1	1.5	-	10
FHP regions	1	-	2	5.5

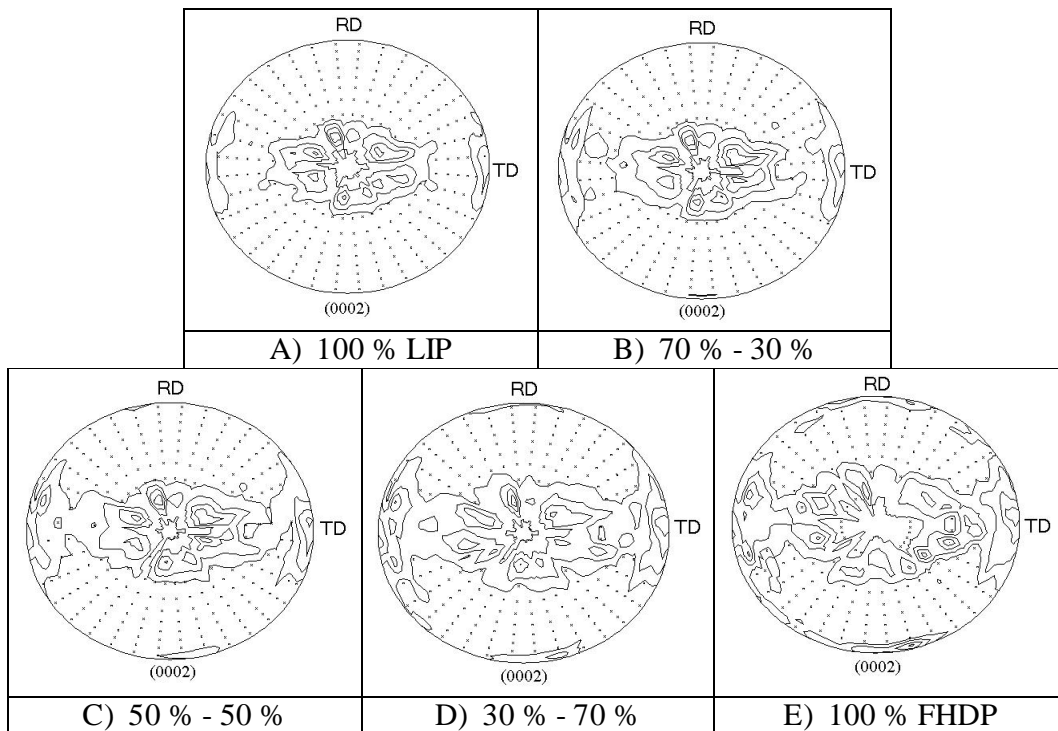Table 2 : CRSS values in the LIP/FHDP model.

Figure 8 : Calculated PSC (0002) pole figures for various proportions of LIP / FHDP regions. FHDP volume fraction increases from (A) to (E).

The calculated (0002) pole figures are shown in Figure 8 for various relative volume fractions of the two classes of grains. Increasing the FHDP volume fraction leads

Mathematical Modeling in Metal Processing and Manufacturing (CD-ROM),
P. Martin and W.J. Liu, S. MacEwen, Y. Verreman and J. Goldak eds.
The Metallurgical Society of CIM, Canada, 2000.

to stronger "T" texture components. The calculation indicates that the pyr<c+a> activity increases with strain, and results in an "A" texture component, i.e. c-axes close to the Rolling Direction RD.

III.3. Extrusion Textures

Using the set of CRSS presented in Table 2 it is possible to calculate textures at various thickness levels of an extruded tube. Of course, the calculation only takes into account the effect of the precipitates structure, and not the thermally activated processes.
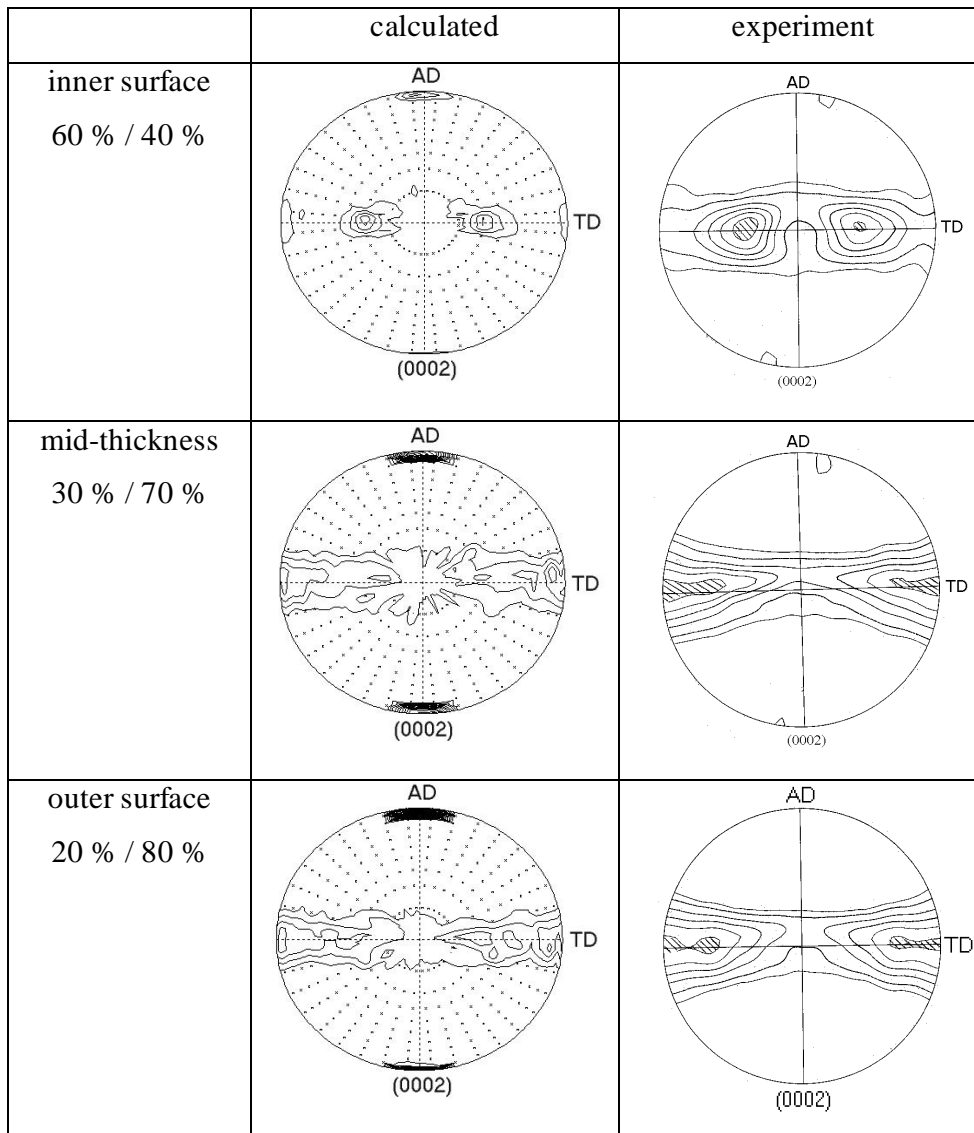
	calculated	experiment
inner surface 60 % / 40 %	AD / TD / (0002)	AD / TD / (0002)
mid-thickness 30 % / 70 %	AD / TD / (0002)	AD / TD / (0002)
outer surface 20 % / 80 %	AD / TD / (0002)	AD / TD / (0002)

Figure 9 : Calculated and experimental extrusion textures. The LIP / FHP regions volume fractions are chosen according to the cooling rate during β-quenching.

Mathematical Modeling in Metal Processing and Manufacturing (CD-ROM),
P. Martin and W.J. Liu, S. MacEwen, Y. Verreman and J. Goldak eds.
The Metallurgical Society of CIM, Canada, 2000.

The deformation path was quantitatively evaluated using an Eulerian finite element formulation such as LAM3 (23) and assuming a steady-state flow. Knowing the friction coefficients between the die and the material, a sequence of velocity gradients was calculated along various streamlines (24). The texture evolution was then computed along streamlines at the inner and outer surfaces of the tubes and at mid-thickness. The results are presented in Figure 9 and compared to experimental measurements. Bearing in mind that the cylinder should display a microstructure gradient, the relative volume fractions of LIP and FHDP regions were varied along the radius of the tube.

Figure 9 shows that the calculation can reasonably reproduce the c-axes distribution in the plane perpendicular to the axial direction AD. However, the "A" texture component associated with c-axes close to AD is not found experimentally. As explained in section III.2 for the PSC tests, this "A" component is generated by the pyr<c+a> activity in the FHDP regions, at large deformations. The intensity level appears very high because all the grains take almost exactly the same orientation. However, even along the outer surface where the FHDP/LIP ratio is maximum, the "A" texture component does not represent more than 23 % of the total volume fraction.

IV. DISCUSSION

IV.1. Effect of Metadynamic Recrystallization

Given the results of section III.3, it is assumed that the "A" texture component is removed after extrusion, due to metadynamic recrystallization. This assumption is further supported by several experimental facts, as presented below.

a) The PSC textures in Figure 4(B) (RQ sample, deformed at 923K) and Figure 4(C) (RQ sample, deformed at 1023 K) show that the "A" orientations have disappeared while recrystallization appeared.

b) Annealing experiments have been performed on extruded samples only partially recrystallized (i.e.: recrystallized fractions of about 50 %). The annealed textures show a significant weakening of "A"-type texture components while the distribution of c-axes in the Radial-Tangent (RD-TD) plane remained about the same.

c) An extrusion process has been stopped while the material was still flowing inside the extrusion die. The material cooled down because of heat conduction, and the cooling rate was in turn faster than the one induced by air convection. Using TEM it was checked that such a cooling rate prevented recrystallization. The associated texture measurements show a pronounced "A" texture component.

A tentative explanation of the Zircaloy-4 recrystallization behavior may be given in terms of the theory developed by (25) which, so far, has been used only for cubic

materials, e.g. (26). The model is based on the assumption that the nuclei that would grow during recrystallization will have orientations minimizing the elastic energy related to the dislocations stress field in the surrounding parent grain. This stress field is considered to be of highest intensity in the direction parallel to the average Burgers vector direction. To minimize the energy, a growing nucleus will have its minimum Young's modulus direction aligned with the direction of maximum stress. In zirconium in the temperature range of interest, the Young's modulus is minimum in the basal plane and maximum along the c-axis (1). The ratio of maximum to minimum is approximately 2. According to the model, only when a non-negligible pyr<c+a> activity has occurred would c-axis reorientation take place during recrystallization. Since we know this is the case for "A"-oriented grains, it is not surprising to see them disappear during recrystallization.

IV.2. Precipitation and Slip Activity

We discuss here the physical reasons for the differences in CRSS for FHDP and LIP regions, on the basis of previous work reported in the literature.

At low temperature, the effect of oxygen on the active deformation modes in titanium has been shown to favor pyramidal slip (27-29). On the other hand, in cold rolled Zr and Zircaloy, cross slip from a prismatic to a pyramidal plane with a common <a>-Burgers vector was observed by (30) using TEM. Further, this cross slip was more active with increasing oxygen content. It was also noted that pyr<c+a> glide was frequent when twinning did not occur. These results suggest that the effect of interstitial oxygen is similar in zirconium and titanium alloys.

Dynamic strain aging has been reported in Zircaloy-4 over the temperature range we are concerned with (31). It was shown that the extent of this phenomenon was inversely proportional to the amount of iron in the second-phase particles (31). Also, *a finer dispersion and smaller volume fraction* of these particles, i.e. a **FHDP** microstructure in our vocabulary, were found to promote strain aging.

We conclude that FHDP regions might be those where the mean diffusion length of Fe atoms, released from the precipitates, is comparable to the average precipitate spacing. Most of the volume fraction of the material is then influenced by diffusing Fe atoms. Since they can interact with moving dislocations, they can also modify the relative CRSS, as oxygen does at lower temperature. Their assumed effect is to make pyramidal slip easier, and to inhibit basal slip.

IV.3. The Extended Polycrystalline Model

The LIP/FHDP model presented in section III had the primary purpose to support the SEM and TEM studies of section II.3, made on extruded samples. It showed that, even when no recrystallization takes place as in the PSC tests, the distinction between LIP and FHDP regions is useful and allows to explain the observed microstructure dependency of

texture evolution. In other words, the conclusion that LIP and FHDP grains evolve towards different texture components was not influenced by the effects of thermally activated processes.

A grain subdivision mechanism has been described in section II.3.2, where the platelet structure splits up with deformation into "cells" of increasing misorientation, thereby transforming those cells into real grains. Such a phenomenon has been observed in other materials, e.g. (32), and is designated as "extended recovery" or "continuous recrystallization". Unlike *discontinuous* recrystallization this phenomenon does not prevent the formation of pronounced textures and its effects on the texture evolution have therefore not been explicitly considered. However, the resulting highly misoriented substructure allows to approximate the immediate neighborhood properties of the grains by the polycrystal properties (see Figure 7), and to validate the so-called 1-site approximation in the self-consistent model (17).

Finally, one should note that the proposed LIP/FHDP model for Widmanstätten structures has introduced an additional degree of freedom, namely the volume fraction of FHDP regions. It may be argued that this volume fraction represents a fitting parameter. However, the FHDP volume fraction may be evaluated as a direct function of the cooling rate during β-quenching and of subsequent annealing time. We believe that a single value can be used for a given microstructure to simulate various deformation modes, including the more complex ones such as extrusion. For example, the FDHP volume fractions reported in Figure 9 have shown a good agreement with those assessed from torsion tests, where we took advantage of the axial effects resulting from the texture-induced anisotropy. The latter procedure will be discussed in a future paper.

V. CONCLUSIONS

In this study we have shown that microstructure considerations may become very important for the control of texture evolution in high temperature forming processes involving zirconium-based alloys. The role of β–quenching prior to deformation is emphasized, both in terms of microscopic deformation modes and texture evolution. A LIP/FHDP model is presented and calculated texture evolution agrees with experimental measurements for plane strain compression laboratory tests. The same model is used to predict hot extrusion textures at different thickness levels of the tubes, and suggests an effect of metadynamic recrystallization on the deformation-induced texture.

A detailed explanation of the influence of the precipitate structure on high temperature texture evolution of zirconium-based alloys is still needed. A few clues have been proposed, based on existing work, and are consistent with the LIP/FHDP model. It is clear, however, that the phenomenological approach adopted here, essentially based on the variation of CRSS values, should be confirmed and/or improved by additional appropriate microscopic observations associated with intra-crystalline modeling.

VI. REFERENCES

1.　P.A. Turner, N. Christodoulou and C.N. Tomé, Int. J. Plast. Vol 11, 1995, 251.

2.　A. Akhtar, J. Nucl. Mater. Vol. 47, 1973, 79.

3.　B.A. Cheadle and C.E. Ells, *J. Nucl. Mater*. **24**, pp. 240-244, 1967.

4.　B.A. Cheadle, S.A. Aldridge and C.E. Ells, J. Nucl. Mater. Vol 34, 1970, 119.

5.　R.A. Lebensohn, P.V. Sanchez and A.A. Pochettino, Scripta metall. mater. Vol 30, 1994, 481.

6.　E.D. Hindle and G.F. Slattery, J. Inst. Metals Vol 93, 1965, 565.

7.　E. Tenckhoff and P.L. Rittenhouse, Applications-Related Phenomena for Zirconium and its Alloys, ASTM STP 458, 1969, 50-67.

8.　B.A. Cheadle, S.A. Aldridge and C.E. Ells, Canadian Metallurgical Quarterly Vol 11, 1972, 121-127.

9.　R.A. Holt and S.A. Aldridge, J. Nucl. Mater. Vol 135, 1985, 246-259.

10.　Cezus Company Internal Report.

11.　A. Akhtar, Acta Metall. Vol 21, 1973, 1.

12.　L. Xiao and H. Gu, Met. Mater. Trans. A Vol. 28A, 1997, 1021-1033.

13.　J.K. Chakravartty, S. Banerjee, Y.V.R.K. Prasad and M.K. Asundi, J. Nucl. Mater. Vol 187, , 1992, 260-271.

14.　R.D. Doherty, D.A. Hughes, F.J. Humphreys, J.J. Jonas, D. Juul Jensen, M.E. Kassner, W.E. King, T.R. McNelley, H.J. McQueen and A.D. Rollett, Mater. Sci. Eng. Vol A238, 1997, 219-274.

15. K. Loucif, R. Borrelly and P. Merle, J. Nucl. Mater. Vol 210, 1994, 84-96.

16. D. Ciurchea, A.V. Pop, C. Gheorghiu, I. Furtuna, M. Todica, A. Dinu and M. Roth, J. Nucl. Mater. Vol 231, 1996, 83-91.

17. R.A. Lebensohn and C.N. Tomé, Acta Metall. Mater. Vol 41, 1993, 2611-2624.

18. A. Akhtar, Met. Trans. A, Vol 7A, 1976, 1735-1741.

19. A.B. Watts and H. Ford, Proceedings Instit. Mech. Engineers Vol 169, 1955, 1141-1149.

20. S. Zaefferer and R.A. Schwarzer, Materials Science Forum, Vols 157-162, 1994, 241-246.

21. C.N. Tomé, R.A. Lebensohn and U.F. Kocks, Acta metall. Mater. Vol 39, 1991, 2667-2680.

22. J.W. Signorelli, R.E. Logé, Y.B. Chastel and R.A. Lebensohn, Model. Simul. Mater. Sc. Eng., Vol. 8, 2000, 193-209.

23. A. Hacquin, Thèse Ecole Nationale Supérieure des Mines de Paris, 1996.

24. R.E. Logé, Thèse Ecole Nationale Supérieure des Mines de Paris (France), 1999.

25. D.N. Lee, Scripta Metall. Mater. Vol 32, 1995, 1689-1694.

26. C-H. Choi and D.N. Lee, Met. Mater. Trans. A, Vol 28A, 1997, 2217-2222.

27. A.T. Churchman, Proc. R. Soc., Vol. A226, 1954, 216-226.

28. G. Welsch and W. Bunk, Metall. Trans. A, Vol 13A, 1982, pp. 889-899.

29. J.S. Lecomte, M.J. Philippe and P. Klimanek, Mater. Sci. Eng. Vols A234-236, 1997, 869-872.

30. M.J. Philippe, C. Esling and B. Hocheid, Text. Microstr. Vol 7, 1988, 265-301.

31. A.M. Garde, J. Nucl. Mater. Vol 80, 1979, 195-206.

32. S. Gourdet, A. Girinon and F. Montheillet, Thermec'97, Wollongong NSW, Australia, ed. by T. Chandra and T. Sakai, 1997, 2117-2124.